The Astrophysical Journal, 904:29 (6pp), 2020 November 20 https://doi.org/10.3847/1538-4357/abbb32

Screening Effects on Electron Capture Rates and Type Ia Supernova Nucleosynthesis

Kanji Mori[1,2,8], Toshio Suzuki[2,3], Michio Honma[4], Michael A. Famiano[2,5], Toshitaka Kajino[1,2,6], Motohiko Kusakabe[6], and A. Baha Balantekin[2,7]
[1] Graduate School of Science, The University of Tokyo, 7-3-1 Hongo, Bunkyo-ku, Tokyo, 113-0033, Japan
[2] Division of Science, National Astronomical Observatory of Japan, 2-21-1 Osawa, Mitaka, Tokyo 181-8588, Japan
[3] Department of Physics, College of Humanities and Sciences, Nihon University, 3-25-40 Sakurajosui, Setagaya-ku, Tokyo 156-8550, Japan
[4] Center for Mathematical Sciences, University of Aizu, Tsuruga, Ikki-machi, Aizu-Wakamatsu, Fukushima 965-8580, Japan
[5] Department of Physics, Western Michigan University, Kalamazoo, MI 49008, USA
[6] School of Physics, Beihang University, 37 Xueyuan Road, Haidian-qu, Beijing 100083, People's Republic of China
[7] Department of Physics, University of Wisconsin–Madison, Madison, WI 53706, USA
Received 2020 July 27; revised 2020 September 22; accepted 2020 September 22; published 2020 November 19

Abstract

Type Ia supernovae (SNe Ia) are believed to be a thermonuclear explosion of a white dwarf, but the mass of their progenitors is still an open problem. In near-Chandrasekhar-mass (near-$M_{\rm Ch}$) models of SNe Ia, the central density reaches $\gtrsim 10^9$ g cm^{-3}. The electron chemical potential becomes higher than the Q-values of electron capture (EC) transitions between *fp*-shell nuclei, so a portion of the available electrons is captured by iron group elements and thus neutron-rich isotopes are formed. Since EC reaction rates are sensitive to the density, the degree of neutronization is a key to distinguish near- and sub-$M_{\rm Ch}$ models. In order to compare observations and theoretical models, an accurate treatment of EC reactions is necessary. In previous theoretical works, however, effects of electron screening on ECs are ignored. Screening lowers EC rates and thus leads to a higher electron fraction. We implement electron screening on ECs to calculate explosive SN Ia nucleosynthesis in a near-$M_{\rm Ch}$ single degenerate model. It is found that some of neutron-rich nuclear abundances, namely, those of ^{46,48}Ca, ^{50}Ti, ^{54}Cr, ^{58}Fe, ^{64}Ni, and ^{67,70}Zn, decrease when screening effects on ECs are considered. Of these, ^{50}Ti, ^{54}Cr, and ^{58}Fe are particularly interesting because a significant portion of the solar abundance of these nuclei is presumed to originate from SNe Ia. We conclude that implementing the screening effect on ECs in modern SN Ia models is desirable to precisely calculate abundances of neutron-rich nuclides.

Unified Astronomy Thesaurus concepts: Explosive nucleosynthesis (503); Type Ia supernovae (1728)

Supporting material: tar.gz file

1. Introduction

Explosive nucleosynthesis in Type Ia supernovae (SNe Ia) is a major source of iron group elements in the Galaxy, but the nature of their progenitor is still under debate. Proposed models of SN Ia progenitors are classified into two regimes. In near-Chandrasekhar-mass (near-$M_{\rm ch}$) models (e.g., Whelan & Iben 1973; Iben & Tutukov 1984), carbon fusion is ignited in a white dwarf (WD) when its mass gets close to $M_{\rm ch}$. On the other hand, in sub-$M_{\rm ch}$ models (e.g., Woosley & Weaver 1994; Guillochon et al. 2010), an SN explosion is triggered even if a WD is lighter than $M_{\rm ch}$.

Electron capture (EC) reactions play a key role in each model. In near-$M_{\rm ch}$ models, more neutron-rich isotopes are produced because of the high central density $\gtrsim 10^9$ g cm^{-3}. Abundances of neutron-excess isotopes have been measured in astronomical observations. X-ray observations of SN Ia remnants Kepler (Park et al. 2013), Tycho (Yamaguchi et al. 2014), and 3C 397 (Yamaguchi et al. 2015) have been performed to estimate the nickel and manganese abundances. Also, late-time light curves of SN 2011fe (Shappee et al. 2017; Dimitriadis et al. 2017), 2012cg (Graur et al. 2016), 2013aa (Jacobson-Galán et al. 2018), 2014J (Yang et al. 2018; Li et al. 2019), and 2015F (Graur et al. 2018) can be used to estimate the abundances of ^{57}Co and ^{55}Fe, assuming that they are powered by the decay chains of isobar mass numbers $A = 57$ and $A = 55$ (Seitenzahl et al. 2009). In order to understand the origin of SNe Ia, it is necessary to accurately calculate abundances of neutron-rich nuclei and compare the models with the observations.

The measurement of EC rates of fully stripped unstable nuclei is all but impossible, so nuclear shell models have been adopted to calculate them theoretically (Fuller et al. 1982a, 1982b; Dean et al. 1998; Langanke & Martínez-Pinedo 2001; Honma et al. 2004, 2005). Although the shell models have gradually become more sophisticated, only bare EC rates have been used as an input to SN Ia models (e.g., Iwamoto et al. 1999; Brachwitz et al. 2000; Parikh et al. 2013; Mori et al. 2016, 2018; Bravo 2019). However, since nuclear reactions in SNe occur in ionized plasma, electron screening changes effective nuclear reaction rates. Such effects have been considered only for thermonuclear charged particle reaction rates (Salpeter 1954; Dewitt et al. 1973; Graboske et al. 1973; Famiano et al. 2016). Effects of screening on ECs have not been estimated in SNe Ia, though they have been explored in Big Bang nucleosynthesis (Luo et al. 2020) and SNe II (Famiano et al. 2020). These potentially affect neutronization in SNe Ia remarkably.

We therefore perform calculations of SN Ia nucleosynthesis with screened EC rates. This paper is organized as follows. In Section 2, we explain the method to calculate the effect of screening on ECs and the adopted SN Ia models. In Section 3, we compare the results of SN Ia nucleosynthesis calculations with and without electron screening with each other. These results are discussed and summarized in Section 4.

[8] Research Fellow of Japan Society for the Promotion of Science.

2. Method

2.1. Electron Capture Rates

The EC rates in stellar environments are evaluated as (Fuller et al. 1982a, 1982b; Langanke & Martínez-Pinedo 2001; Suzuki et al. 2011)

$$\lambda = \frac{\ln 2}{6146(\mathrm{s})} \sum_i W_i \sum_j (B_{ij}(GT) + B_{ij}(F)) \Phi^{ec},$$
$$\Phi^{ec} = \int_{\omega_{\min}}^{\infty} \omega p (Q_{ij} + \omega)^2 F(Z, \omega) S_e(\omega) d\omega,$$
$$Q_{ij} = (M_p c^2 - M_d c^2 + E_i - E_f)/m_e c^2,$$
$$W_i = \frac{(2J_i + 1) e^{-E_i/kT}}{\sum_i (2J_i + 1) e^{-E_i/kT}}, \quad (1)$$

where $\omega(p)$ is electron energy (momentum) in units of $m_e c^2$ ($m_e c$), m_e is the electron mass, M_p and M_d are nuclear masses of parent and daughter nuclei, respectively, and E_i (E_f) is the excitation energy of the initial (final) state. Here, $B(GT)$ and $B(F)$ are Gamow–Teller and Fermi transition strengths, respectively, given by

$$B_{ij}(GT) = \left(\frac{g_A}{g_V}\right)^2 \frac{1}{2J_i + 1} |\langle f || \sum_k \sigma^k t_+^k || i \rangle|^2,$$
$$B_{ij}(F) = \frac{1}{2J_i + 1} |\langle f || \sum_k t_+^k || i \rangle|^2, \quad (2)$$

where J_i is the total spin of initial state and $t_+ |p\rangle = |n\rangle$. $F(Z, \omega)$ is the Fermi function and $S_e(\omega)$ is the Fermi–Dirac distribution for electrons, with the chemical potential determined at high densities, electron fraction, and temperature, indicated by ρY_e, Y_e, and T, respectively. The chemical potential is determined by

$$\rho Y_e = \frac{1}{\pi^2 N_A} \left(\frac{m_e c}{\hbar}\right)^3 \int_0^{\infty} (S_e - S_p) p^2 dp,$$
$$S_\ell = \frac{1}{\exp\left(\frac{E_\ell - \mu_\ell}{kT}\right) + 1}, \quad (3)$$

where $\ell = e$ for electrons and p for positrons and $\mu_p = -\mu_e$ is the positron chemical potential.

Here, the Coulomb corrections on the transition rates due to the electron background are studied. The screening effects on both electrons and ions are taken into account for the Coulomb effects (Juodagalvis et al. 2010; Toki et al. 2013; Suzuki et al. 2016). The screening effects of electrons are evaluated by using the dielectric function obtained by relativistic random phase approximation (RPA; Itoh et al. 2002). The effect is included by reducing the chemical potential of electrons by an amount equal to the modification of the Coulomb potential at the origin $V_s(0)$ (Juodagalvis et al. 2010), where

$$V_s(r) = Ze^2 (2k_F) J(r),$$
$$J(r) = \frac{1}{2k_F r} \left(1 - \frac{2}{\pi} \int \frac{\sin(2k_F q r)}{q \epsilon(q, 0)} dq\right). \quad (4)$$

Here, $\epsilon(q,0)$ is the static longitudinal dielectric function at zero frequency, and $q = k/2k_F$ with k and k_F the electron wavenumber and Fermi wavenumber, respectively. The modification to the Coulomb potential $J(r)$ is tabulated in Itoh et al. (2002).

The other Coulomb effect is caused by the screening of the ions in the electron background. The threshold energy is modified by

$$\Delta Q_C = \mu_C(Z - 1) - \mu_C(Z), \quad (5)$$

where $\mu_C(Z)$ is the Coulomb chemical potential of the nucleus with charge number Z (Slattery et al. 1982; Ichimaru 1993). The Coulomb chemical potential in a plasma of electron number density n_e and temperature T is given by

$$\mu_C(Z) = kTf(\Gamma), \quad (6)$$

with $\Gamma = Z^{5/3} \Gamma_e$, $\Gamma_e = \frac{e^2}{kTa_e}$, and $a_e = \left(\frac{3}{4\pi n_e}\right)^{1/3}$. The function f for the strong-coupling regime, $\Gamma > 1$, is given by Equation (A.48) in Ichimaru (1993), while for the weak-coupling regime, $\Gamma < 1$, an analytic function given by Yakovlev & Shalybkov (1989) is used (see also Equation (A.6) in Juodagalvis et al. 2010). The threshold energy is enhanced for EC processes, and the EC (β-decay) rates are reduced (enhanced) by the Coulomb effects.

The EC rates for the *pf*-shell in stellar environments are evaluated with the use of the shell-model Hamiltonian, GXPF1J (Honma et al. 2005), which is a modified version of GXPF1 (Honma et al. 2004). The quenching of the axial-vector coupling constant is taken to be $g_A^{\mathrm{eff}}/g_A = 0.74$ (Caurier et al. 2005). Transitions from the states with excitation energies up to $E_X = 2$ MeV are taken into account. Here, the experimental data such as excitation energies for excited states in both parent and daughter nuclei and $B(GT)$ values are taken into account when they are available in the online retrieval system of the National Nuclear Data Center.[9] Calculated *e*-capture rates for ^{56}Ni (e^-, ν) ^{56}Co with and without the screening effects are shown in Figure 1. The weak rates for the case with the screening effects are found to be reduced by about 20%–40% compared with those without the screening effects.

2.2. Nucleosynthesis Calculation

Because nucleosynthesis in sub-M_{ch} models is nearly as sensitive to EC rates (Bravo 2019), we focus on near-M_{ch} models. The physical mechanism of propagation of the burning front in SNe Ia is still unclear (e.g., Niemeyer 1999; Branch & Wheeler 2017). We adopt two one-dimensional near-M_{ch} models with different burning schemes. One is W7 (Nomoto et al. 1984), which is a widely used deflagration model, and the other is WDD2 (Iwamoto et al. 1999), which is a delayed-detonation model. These models adopt the equation of state in Slattery et al. (1982) and Slattery et al. (1980), which take the Coulomb correction into account. Since the critical density of the deflagration–detonation transition is not known (Niemeyer & Kerstein 1997), it is assumed to be 2.2×10^7 g cm^{-3} in WDD2. The time evolution of the central temperature T_c and density ρ_c of the models is shown in Figure 2.

We performed nuclear reaction network calculations as a postprocess with W7 and WDD2 using `libnucnet` (Meyer & Adams 2007). The initial composition is $X(^{12}\mathrm{C}) = 0.475$, $X(^{16}\mathrm{O}) = 0.50$, and $X(^{22}\mathrm{Ne}) = 0.025$, where $X(i)$ is the mass fraction of each nucleus i. The network calculation is

[9] https://www.nndc.bnl.gov/

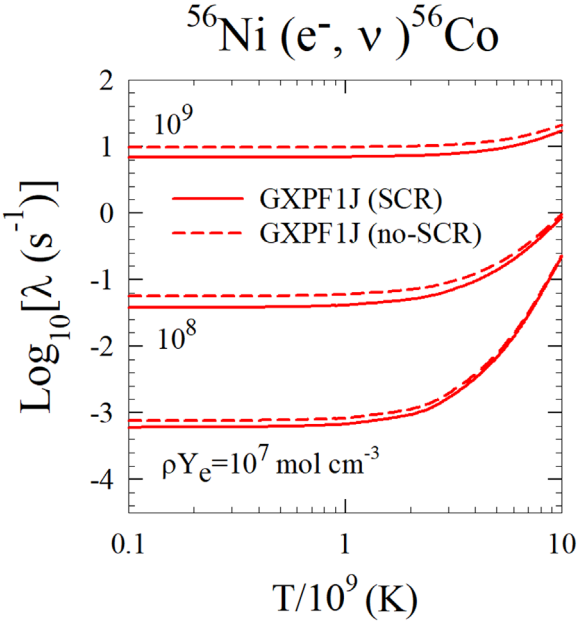

Figure 1. Comparison of calculated *e*-capture rates for ^{56}Ni (e^-, ν) ^{56}Co obtained with the GXPF1J at densities $\rho\, Y_e = 10^7$, 10^8, and 10^9 mol cm^{-3} for temperatures $T = 10^8$–10^{10} K. Solid and dashed curves denote the rates with and without the screening effects, respectively.

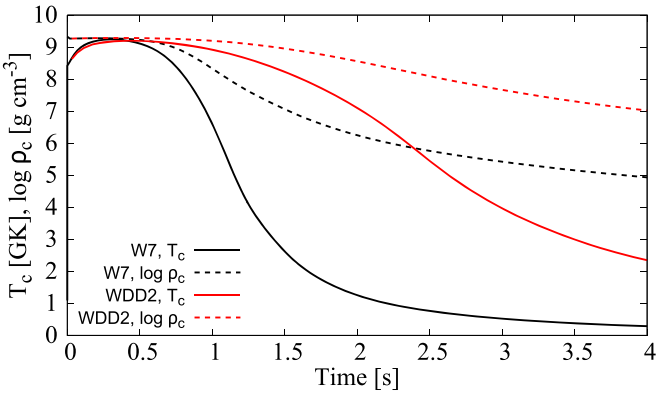

Figure 2. Time evolution of the central temperature T_c and density ρ_c. The black lines show the W7 model, and the red lines show the WDD2 model. The solid lines show T_c and the broken lines show ρ_c.

performed until 100 s after the ignition at the WD center, and after that unstable nuclei are forced to decay. The network includes 5441 nuclear species up to astatine. Thermonuclear reaction rates are taken from the JINA REACLIB v1.1 database (Cyburt et al. 2010). EC rates of *fp*-shell nuclei are calculated from the GXPF1J shell model (Honma et al. 2005). The EC rates of other nuclei are taken from Oda et al. (1994) and Fuller et al. (1982a, 1982b). The treatment of electron screening for thermonuclear reactions is based on Wallace et al. (1982). Screened EC rates for *pf*-shell nuclei are treated as we explain in Section 2.1, and the screening effect on EC rates for other nuclei is not considered. The EC rates are tabulated in a range $\rho\, Y_e = 10^5$–10^{11} mol cm^{-3} and $T = 10^7$–10^{11} K (Honma & Suzuki 2020). The `libnucnet` calculates the effective *ft*-values (Fuller et al. 1985) from the tabulated rates and interpolates $\log ft$ as a linear function of T and $\log \rho$ to perform the network calculation.

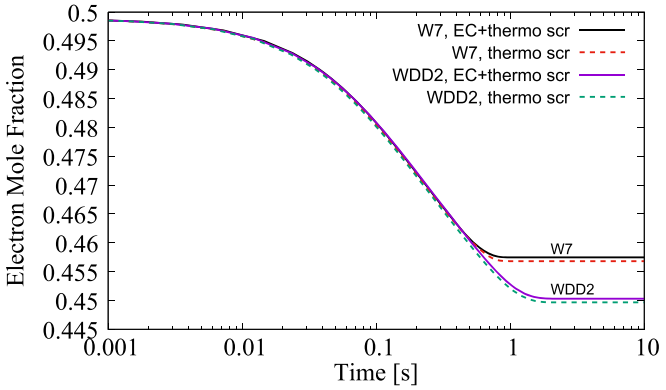

Figure 3. Time evolution of the electron fraction at the center of the SN Ia models. The solid lines indicate the result with the screening effect on both ECs and thermonuclear reactions, while the broken lines indicate the result with the screening effect only on thermonuclear reactions.

3. Results

Using the modifications to the EC capture rates previously computed, the W7 and WDD2 thermodynamic trajectories were used to compute the final nuclear abundances in each model.

3.1. W7 Model

The neutronization degree of plasma can be represented by the electron fraction $Y_e = \sum_i Z_i Y_i$, where Z_i is the atomic number and Y_i is the mole fraction of the ith nuclear species. Thus, for equal numbers of neutrons and protons, Y_e is exactly 0.5. If the number of neutrons exceeds that of protons, Y_e becomes lower than 0.5.

Figure 3 shows the time evolution of Y_e at the center of the explosion. The solid lines indicate the results with the screening effect on both ECs and thermonuclear reactions, while the broken lines indicate the results with the screening effect only on thermonuclear reactions.

In our models, the initial electron fraction is $Y_e = 0.49886$, which is slightly lower than 0.5 because of the abundance of the neutron-rich nucleus ^{22}Ne in the initial composition. The EC reactions freeze out after ∼1 s of the explosion. It is seen that the screened lower EC rates results in a higher Y_e. The electron fraction at 10 s is $Y_e = 0.45747$ if screening on ECs is considered, while $Y_e = 0.45682$ if screening only on thermonuclear reactions is considered.

It is known that neutronization in the central region of a WD is determined by the EC on protons (e.g., Bravo 2019). Although the screening effect on the EC of protons is not considered in the present work, we checked that the change in the EC rate of protons is within 1%. This is because the electric charge of protons is smaller than those of *fp*-shell nuclei. When we consider the screening effect on free protons, the central electron fraction is $Y_e = 0.45751$. This value is slightly higher than the one shown in the previous paragraph, but it does not lead to qualitative differences in abundances.

Figure 4 shows a comparison of the nucleosynthetic yields in the cases with and without the screening effect on ECs. One can find that the abundances of neutron-rich isotopes are smaller when the screening effect on ECs is considered. Most notably, the abundances of ^{48}Ca, ^{50}Ti, ^{54}Cr, ^{58}Fe, ^{64}Ni, and ^{70}Zn are 30%–50% smaller.

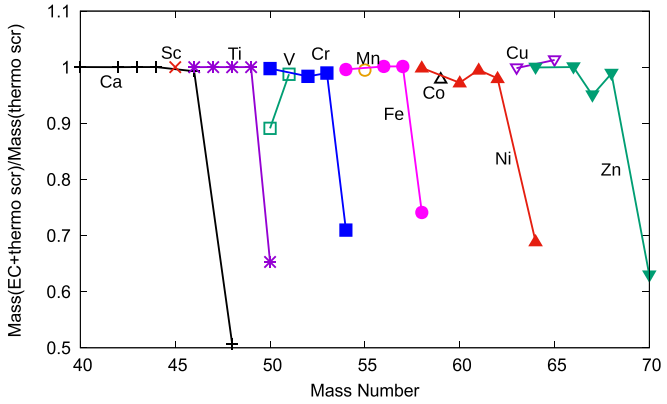

Figure 4. Abundance ratios with and without screening on ECs. W7 is adopted as an SN Ia model.

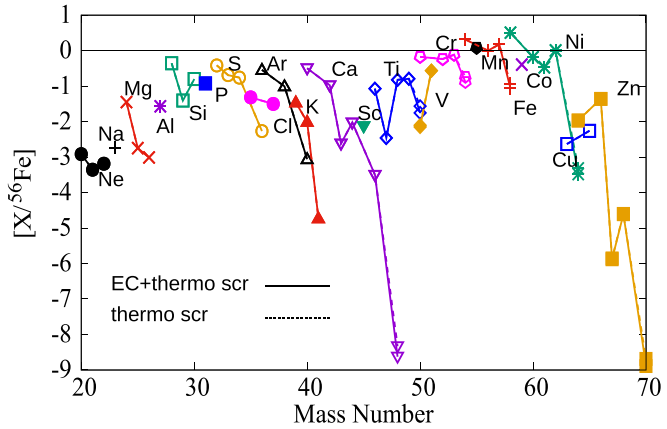

Figure 5. Abundances normalized by the solar and ^{56}Fe abundances. The solid lines adopt screening on ECs and the broken lines do not. W7 is adopted as an SN Ia model.

Figure 5 shows the SN Ia yields normalized to the solar abundances. The normalized abundance $[X/^{56}\mathrm{Fe}]$ for a nuclide X is defined as

$$[X/^{56}\mathrm{Fe}] = \log\left(\frac{Y(X)}{Y(^{56}\mathrm{Fe})}\right) - \log\left(\frac{Y_{\odot}(X)}{Y_{\odot}(^{56}\mathrm{Fe})}\right), \quad (7)$$

where $Y(i)$ and $Y_{\odot}(i)$ are respectively the number abundances in the SNe Ia models and in the solar system of species i (Lodders 2020). The solid lines show the result in the case with the screening effect on ECs, while the dashed lines indicate results without EC screening. In an SN Ia, as much as $\sim 0.8 M_{\odot}$ of iron group elements can be produced, while only $\sim 0.1 M_{\odot}$ is produced in a core-collapse SN. For a Galactic SNe Ia event rate of $(\sim 0.54 \pm 0.12)$/century and a core-collapse SNe event rate of $(\sim 2.30 \pm 0.48)$/century (Li et al. 2011), it is expected that $\sim$65% of the iron group elements originates from SNe Ia. For the neutron-rich nuclides, production is affected by screening of ECs. The contribution of SNe Ia to the solar abundance of ^{48}Ca, ^{50}Ti, ^{64}Ni, and ^{70}Zn is negligible. However, $[^{54}\mathrm{Cr}/^{56}\mathrm{Fe}]$ and $[^{58}\mathrm{Fe}/^{56}\mathrm{Fe}]$ reach ~ -1. This implies that the contribution of SNe Ia for these nuclei can be as high as $\sim$5%–10%. The contribution of SNe Ia to the solar abundances of these nuclei is summarized in Table 1. The abundances of ^{54}Cr and ^{58}Fe are significantly affected by screening of ECs. It is therefore remarkably important to consider its effect in discussing the origins of these nuclei.

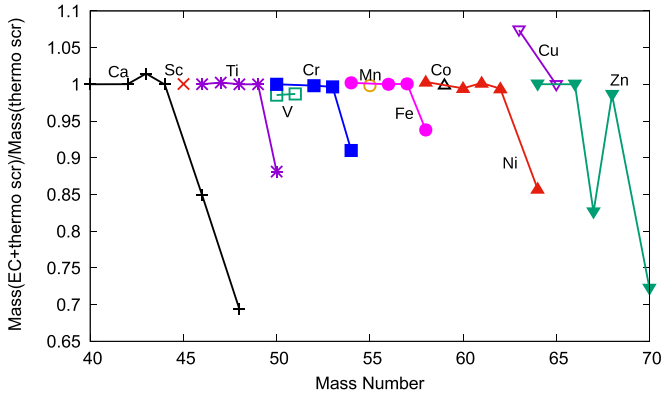

Figure 6. Abundance ratios between the cases with and without screening on ECs. WDD2 is adopted as an SN Ia model.

Table 1
Contribution of SNe Ia to the Solar Abundances in Units of Percent

	^{50}Ti	^{54}Cr	^{58}Fe
EC+thermo scr	1.2 ± 0.2	8.5 ± 1.2	5.7 ± 0.8
thermo scr	1.8 ± 0.3	12 ± 2	7.6 ± 1.1

Note. The W7-like explosion is assumed to dominate the whole SN Ia population. The uncertainties are estimated based on errors in Galactic SN rates (Li et al. 2011).

3.2. WDD2 Model

The qualitative effect of screening on the WDD2 model is similar to that of the W7 model. Figure 3 shows the time evolution of Y_e. As seen in W7, the resultant Y_e is higher as a result of EC screening. The electron fraction at $t = 10$ s is $Y_e = 0.45031$ if screening effects on ECs and thermonuclear reactions are considered and $Y_e = 0.44967$ if screening only on thermonuclear reactions is considered.

Figure 6 shows the abundance ratio for cases with and without screening on ECs. It is seen that the abundances of neutron-rich isotopes tend to be smaller if screening on ECs is considered. In particular, the abundances of ^{46}Ca, ^{48}Ca, ^{50}Ti, ^{54}Cr, ^{58}Fe, ^{64}Ni, ^{67}Zn, and ^{70}Zn are 10%–30% smaller.

While the final abundances of almost all nuclei are not affected by the suppressed EC rates, the abundance of ^{63}Cu increases by 7% when screening on ECs is considered. Half of ^{63}Cu is formed by the β^+-decay of ^{63}Zn whose lifetime is 38 minutes. The abundance of ^{63}Zn located on the outer proton-rich side of stable zinc isotopes increases by the suppressed EC rates. As a result, ^{63}Cu production from the ^{63}Zn decays after the SN is larger.

Figure 7 shows the abundances normalized to solar values. The solid lines indicate results corresponding to the case with EC screening, and the dashed lines correspond to screening of thermonuclear reactions only. For the nuclides affected by EC screening, the contribution of SNe Ia to the solar abundances for ^{46,48}Ca, ^{64}Ni, and ^{67,70}Zn is negligibly small. However, the abundances of ^{50}Ti, ^{54}Cr, and ^{58}Fe reach $[^{50}\mathrm{Ti}/^{56}\mathrm{Fe}] = -0.16$, $[^{54}\mathrm{Cr}/^{56}\mathrm{Fe}] = 0.36$, and $[^{58}\mathrm{Fe}/^{56}\mathrm{Fe}] = -0.080$, where screening on ECs is considered. The SN Ia contribution to the solar abundances can be as high as $\sim$50% for ^{50}Ti and ^{58}Fe, and

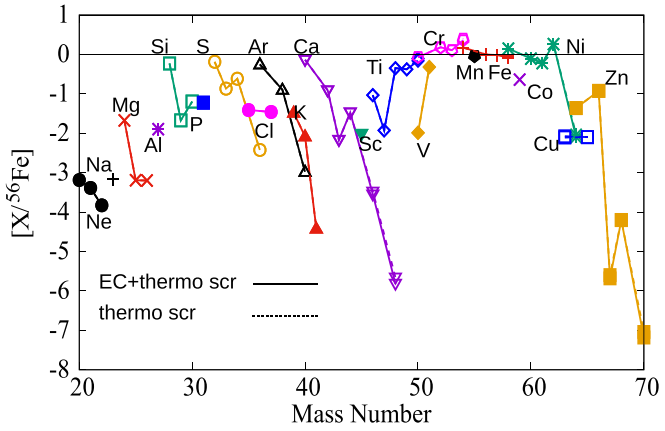

Figure 7. Abundances normalized by the solar and ^{56}Fe abundances. The solid lines adopt screening on ECs and the broken lines do not. WDD2 is adopted as an SN Ia model.

>100% for ^{54}Cr. The overproduction of ^{54}Cr has been reported by previous works (Iwamoto et al. 1999; Mori et al. 2016; Leung & Nomoto 2018) as well. The contribution of SNe Ia for these nuclei is summarized in Table 2.

4. Discussion

In this study, we calculate EC rates of *pf*-shell nuclei and apply them to SN Ia nucleosynthesis. The suppressed EC rates result in smaller Y_e values in SN ejecta and thus smaller abundances of neutron-rich nuclei. The abundances of ^{46,48}Ca, ^{50}Ti, ^{54}Cr, ^{58}Fe, ^{64}Ni, and ^{67,70}Zn are most prominently affected, although the details of the abundance pattern and sensitivity to the EC rates depend on the explosion models. This result is consistent with previous works (Brachwitz et al. 2000; Bravo 2019) that point out strong sensitivity of these nuclei to EC rates.

Screening of ECs does not affect the abundances of isobars with mass numbers of $A = 55$ and 57, which are estimated from late-time light curves of SNe Ia. The effect on the elemental abundances of nickel and manganese, which are estimated in SN remnants, are $\lesssim$0.4% for nickel and $\lesssim$0.5% for manganese.

Of the neutron-rich nuclei that are affected by screening on ECs, ^{50}Ti, ^{54}Cr, and ^{58}Fe are particularly interesting because SNe Ia can significantly contribute to their solar abundances. Since the production of these nuclei depends on the central density (Seitenzahl et al. 2013; Leung & Nomoto 2018), they are a good indicator of the mass of SN Ia progenitors. Hence the information of SN Ia models can be imprinted in the solar abundance patterns of titanium, chromium, and iron. In order to compare the SN Ia models and the observed abundance patterns of these nuclei, we recommend implementing the screened EC rates in modern multidimensional SN Ia models (Jackson et al. 2010; Maeda et al. 2010; Krueger et al. 2012; Seitenzahl et al. 2013; Leung & Nomoto 2018).

The postprocessing technique adopted in this study decouples hydrodynamics from detailed nucleosynthesis. However, since the electron pressure depends on Y_e, changes in EC rates can significantly affect overall dynamics of SNe Ia. For example, incinerated bubbles around the WD center float outward in three-dimensional models, and their motion is dependent on EC rates (Bravo 2019). Also, the spatial extent of the density inversion behind the deflagration front is dependent on EC rates (Timmes & Woosley 1992). These interplays between dynamics and nuclear reactions are not taken into account in the current postprocess calculation for one-dimensional explosion models. It is hence desirable to couple hydrodynamics and the updated EC rates and consider multidimensionality in future studies.

Table 2
Contribution of SNe Ia to the Solar Abundances in Units of Percent

	^{50}Ti	^{54}Cr	^{58}Fe
EC+thermo scr	45 ± 7	150 ± 22	54 ± 8
thermo scr	51 ± 8	165 ± 24	58 ± 9

Note. The WDD2-like explosion is assumed to dominate the whole SN Ia population. The uncertainties are estimated based on errors in Galactic SN rates (Li et al. 2011).

Supplementary data available in data.tar.gz: *e*-capture rates as well as other weak rates (β-decay, e^+-capture, β^+-decay, neutrino energy-loss, and gamma-heating rates) for *pf*-shell nuclei obtained with the GXPF1J with and without the screening (scr) effects are tabulated in a range $\rho Y_e = 10^5$–10^{11} mol cm^{-3} and $T = 10^7$–10^{11} K. Experimental data for the excitation energies of parent and daughter nuclei and $B(GT)$ values are taken into account when they are available in the tables of "rate_obs_scr" and "rate_obs," while purely theoretical values are used in the tables of "rate_scr" and "rate."

This work was supported by JSPS KAKENHI grant Nos. JP19J12892 and JP19K03855. T.K. is supported in part by Grants-in-Aid for Scientific Research of JSPS grant Nos. 20K03958 and 17K05459. A.B.B. is supported in part by the U.S. National Science Foundation grant No. PHY-1806368. M. A.F. is supported by NASA grant #80NSSC20K0498. M.A.F. and A.B.B. acknowledge support from the NAOJ Visiting Professor program. The authors would like to thank IReNA project for the promotion of the compilation and update of nuclear weak rates.

Software: Libnucnet (Meyer & Adams 2007).

ORCID iDs

Kanji Mori https://orcid.org/0000-0003-2595-1657
Toshio Suzuki https://orcid.org/0000-0002-5500-539X
Michael A. Famiano https://orcid.org/0000-0003-2305-9091
Toshitaka Kajino https://orcid.org/0000-0002-8619-359X
Motohiko Kusakabe https://orcid.org/0000-0003-3083-6565
A. Baha Balantekin https://orcid.org/0000-0002-2999-0111

References

Brachwitz, F., Dean, D. J., Hix, W. R., et al. 2000, ApJ, 536, 934
Branch, D., & Wheeler, J. C. 2017, Supernova Explosions: Astronomy and Astrophysics Library (Berlin: Springer-Verlag)
Bravo, E. 2019, A&A, 624, A139
Caurier, E., Martínez-Pinedo, G., Nowacki, F., Poves, A., & Zuker, A. P. 2005, RvMP, 77, 427
Cyburt, R. H., Amthor, A. M., Ferguson, R., et al. 2010, ApJS, 189, 240
Dean, D. J., Langanke, K., Chatterjee, L., et al. 1998, PhRvC, 58, 536
Dewitt, H. E., Graboske, H. C., & Cooper, M. S. 1973, ApJ, 181, 439
Dimitriadis, G., Sullivan, M., Kerzendorf, W., et al. 2017, MNRAS, 468, 3798
Famiano, M., Balantekin, A. B., Kajino, T., et al. 2020, ApJ, 898, 163

Famiano, M. A., Balantekin, A. B., & Kajino, T. 2016, PhRvC, 93, 045804
Fuller, G. M., Fowler, W. A., & Newman, M. J. 1982a, ApJ, 252, 715
Fuller, G. M., Fowler, W. A., & Newman, M. J. 1982b, ApJS, 48, 279
Fuller, G. M., Fowler, W. A., & Newman, M. J. 1985, ApJ, 293, 1
Graboske, H. C., Dewitt, H. E., Grossman, A. S., et al. 1973, ApJ, 181, 457
Graur, O., Zurek, D., Shara, M. M., et al. 2016, ApJ, 819, 31
Graur, O., Zurek, D. R., Rest, A., et al. 2018, ApJ, 859, 79
Guillochon, J., Dan, M., Ramirez-Ruiz, E., et al. 2010, ApJL, 709, L64
Honma, M., Otsuka, T., Brown, B. A., et al. 2004, PhRvC, 69, 034335
Honma, M., Otsuka, T., Mizusaki, T., et al. 2005, JPhCS, 20, 7
Honma, M., & Suzuki, T. 2020, https://www.phys.chs.nihon-u.ac.jp/suzuki/data5/, and supplementary data material
Iben, I., & Tutukov, A. V. 1984, ApJS, 54, 335
Ichimaru, S. 1993, RvMP, 65, 255
Itoh, N., Tomizawa, N., Tamamura, M., & Wanajo, S. 2002, ApJ, 579, 380
Iwamoto, K., Brachwitz, F., Nomoto, K., et al. 1999, ApJS, 125, 439
Jackson, A. P., Calder, A. C., Townsley, D. M., et al. 2010, ApJ, 720, 99
Jacobson-Galán, W. V., Dimitriadis, G., Foley, R. J., et al. 2018, ApJ, 857, 88
Juodagalvis, A., Langanke, K., Hix, W. R., Martínez-Pinedo, G., & Sampaio, J. M. 2010, NuPhA, 848, 454
Krueger, B. K., Jackson, A. P., Calder, A. C., et al. 2012, ApJ, 757, 175
Langanke, K., & Martínez-Pinedo, G. 2001, ADNDT, 79, 1
Leung, S.-C., & Nomoto, K. 2018, ApJ, 861, 143
Li, W., Chornock, R., Leaman, J., et al. 2011, MNRAS, 412, 1473
Li, W., Wang, X., Hu, M., et al. 2019, ApJ, 882, 30
Lodders, K. 2020, Solar Elemental Abundances, in The Oxford Research Encyclopedia of Planetary Science (Oxford: Oxford Univ. Press)
Luo, Y., Famiano, M. A., Kajino, T., Kusakabe, M., & Balantekin, A. B. 2020, PhRvD, 101, 083010
Maeda, K., Röpke, F. K., Fink, M., et al. 2010, ApJ, 712, 624
Meyer, B. S., & Adams, D. C. 2007, M&PSA, 42, 5215
Mori, K., Famiano, M. A., Kajino, T., et al. 2016, ApJ, 833, 179
Mori, K., Famiano, M. A., Kajino, T., et al. 2018, ApJ, 863, 176
Niemeyer, J. C. 1999, ApJL, 523, L57
Niemeyer, J. C., & Kerstein, A. R. 1997, NewA, 2, 239
Nomoto, K., Thielemann, F.-K., & Yokoi, K. 1984, ApJ, 286, 644
Oda, T., Hino, M., Muto, K., et al. 1994, ADNDT, 56, 231
Parikh, A., José, J., Seitenzahl, I. R., et al. 2013, A&A, 557, A3
Park, S., Badenes, C., Mori, K., et al. 2013, ApJL, 767, L10
Salpeter, E. E. 1954, AuJPh, 7, 373
Seitenzahl, I. R., Ciaraldi-Schoolmann, F., Röpke, F. K., et al. 2013, MNRAS, 429, 1156
Seitenzahl, I. R., Taubenberger, S., & Sim, S. A. 2009, MNRAS, 400, 531
Shappee, B. J., Stanek, K. Z., Kochanek, C. S., et al. 2017, ApJ, 841, 48
Slattery, W. L., Doolen, G. D., & Dewitt, H. E. 1980, PhRvA, 21, 2087
Slattery, W. L., Doolen, G. D., & DeWitt, H. E. 1982, PhRvA, 26, 2255
Suzuki, T., Honma, M., Mao, H., Otsuka, T., & Kajino, T. 2011, PhRvC, 83, 044619
Suzuki, T., Nomoto, K., & Toki, H. 2016, ApJ, 817, 163
Timmes, F. X., & Woosley, S. E. 1992, ApJ, 396, 649
Toki, H., Suzuki, T., Nomoto, K, Jones, S., & Hirschi, R. 2013, PhRvC, 88, 015806
Wallace, R. K., Woosley, S. E., & Weaver, T. A. 1982, ApJ, 258, 696
Whelan, J., & Iben, I. 1973, ApJ, 186, 1007
Woosley, S. E., & Weaver, T. A. 1994, ApJ, 423, 371
Yakovlev, D. G., & Shalybkov, D. A. 1989, ASPRv, 7, 311
Yamaguchi, H., Badenes, C., Foster, A. R., et al. 2015, ApJL, 801, L31
Yamaguchi, H., Eriksen, K. A., Badenes, C., et al. 2014, ApJ, 780, 136
Yang, Y., Wang, L., Baade, D., et al. 2018, ApJ, 852, 89